

## INTEGRAL-EQUATION ANALYSIS OF FREQUENCY SELECTIVE SURFACES USING EWALD TRANSFORMATION AND LATTICE SYMMETRY

J. X. Su<sup>\*</sup>, X. W. Xu, M. He, and K. Zhang

Department of Electronic Engineering, Beijing Institute of Technology, Beijing 100081, China

**Abstract**—In this paper, we present the space-domain integral-equation method for the analysis of frequency selective surfaces (FSS), consisting of an array of periodic metallic patches or a metal screens perforated periodically with arbitrarily shaped apertures. The computation of the spatial domain Green's function is accelerated by the Ewald transformation. The geometric model is simplified by the lattice symmetry, so that the unknowns are greatly reduced. Time of filling MOM matrix and solving linear system is dramatically reduced. Our technique shows much higher efficiency when compared with the available commercial software and the existing methods published.

### 1. INTRODUCTION

The frequency selective surfaces (FSS) often consist of an array of periodic metallic patches or a conducting sheet with periodical apertures. It provides uninhibited transmission in specific frequency bands while suppressing transmission in other bands when illuminated by an incident electromagnetic wave. They have found a variety of applications in a broad range of the electromagnetic (EM) spectrum including antenna reflectors, quasi-optical filters, polarizers, switches, and designing more efficient lasers [1]. Recently, it has been shown that periodic structures built from nonmagnetic conducting sheets can exhibit negative real parts of permittivity and permeability [2]. These materials, designated as left-handed metamaterials, are opening new application fields.

Periodic structures are advantageously analyzed with integral-equation (IE) techniques, usually formulated in the spectral domain,

---

*Received 19 August 2011, Accepted 17 October 2011, Scheduled 26 October 2011*

\* Corresponding author: Jianxun Su (sujianxun\_jlgx@163.com).

as exemplified by the case of multilayered FSS [1]. Two approaches can be employed. One is to compute a specific FSS in its entirety [3], the other is to cascade the generalized scattering matrices (GSMs) of the constitutive building blocks [4]. In using the MoM, the appropriate choice of basis function is very important. The entire domain basis functions are often used to analyze the specific geometry, such as dipole, square and so on. For complex shape geometry, subdomain basis functions such as rooftop basis functions [5] and Rao-Wilton-Glisson (RWG) basis functions [6] have to be used. Generally, the former is only utilized to analyze the canonical geometry FSS, and the later is utilized to analyze the arbitrary geometry FSS for its ability to model arbitrarily shaped structures. Therefore, spatial domain integral-equation analysis of periodic structures using RWG basis functions becomes a popular technique.

The application of the Floquet-Bloch theorem [7, 8] reduces the computational domain of infinite periodic structures to a single unit cell but leads to the result that involves the numerical evaluation of very slowly converging series. A number of techniques, either analytical or numerical, have been developed to accelerate the convergence of the relevant series. Among the analytical ones, Poisson's formula and Kummer's decompositions [9] represent the most commonly adopted approaches. Numerical acceleration techniques like the Shanks' transformations [10] or the  $\rho$  algorithm [11] may also be necessary to further accelerate the result. Improved convergence can be obtained by applying the Ewald's transformation [12]. Compared to the other acceleration techniques, Ewald method converges fastest (Gaussian convergence) and is the most accurate when the observation point gets close to the sources. Recently, space-domain integral-equation method [13, 14] and hybrid finite-element/boundary-integral (FE/BI) method [15], using the Ewald transformation to accelerate the convergence of PGF, have been applied to analysis of three-dimensional doubly periodic structures based on arbitrary non-orthogonal lattice configurations.

In this paper, we propose a spatial-domain integral-equation method for the analysis of frequency selective surfaces (FSS) using Ewald transformation and lattice symmetry. The involved PGF are computed using the Ewald transformation to accelerate their convergence. This paper first presents integral-equation method analysis of periodic structure with lattice symmetry, simplifying geometry model of unit cell. Typically, the lattice configuration of periodic structure has good symmetry. If we use the lattice symmetry to simplify the unit model, the unknowns will be reduced greatly, so that the solving time of MoM linear system and the matrix-filling time

are reduced dramatically. Two new basis functions deriving from RWG basis function are introduced to deal with the current condition of the unit patch. This technique will be demonstrated in detail in Section 5.

This paper is organized as follows. Firstly, integral-equation method is described and two new basis functions are introduced. Secondly, Ewald transformation of periodic Green’s function (PGF) and singularity extraction are described. Thirdly, the technique using lattice symmetry to simplify the geometry model is proposed to analyze periodic structure efficiently. Finally, some numerical examples are presented to illustrate the efficiency of our approach.

## 2. INTEGRAL EQUATION

We consider a frequency selective surface with identical metallic objects of arbitrary shape, periodically arranged in the  $xoy$ -plane (Fig. 1). The frequency selective surface has a general skewed lattice defined by primitive vector  $a_1$  and  $a_2$  and is illuminated by a plane wave impinging with the incidence angle  $(\theta^{inc}, \phi^{inc})$ . Let  $S$  designate the surface of the metallic object within the structure’s unit cell. The analysis is based on the solution of the following mixed-potential integral equation (MPIE) [13]:

$$-\hat{n} \times E^{inc} = \hat{n} \times \left[ -j\omega \vec{G}_A \otimes \vec{J} + \frac{1}{j\omega} (\nabla G_V) \otimes (\nabla' \cdot \vec{J}) \right] \quad (1)$$

which is obtained by enforcing the boundary conditions on the PEC surface  $S$ .  $E^{inc}$  is the incident electric field,  $\hat{n}$  is the outside unit normal

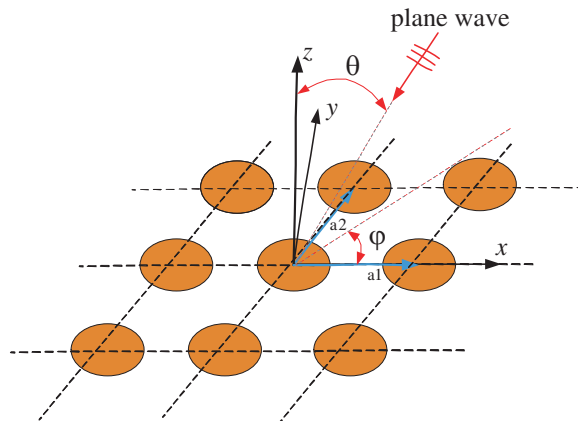


Figure 1. 2-D periodic structure with a general skewed lattice.

to  $S$ ,  $\vec{J}$  is the unknown current density on  $S$ , and  $\vec{G}_A$  and  $G_V$  are the vector and scalar potential GFs that take into account the periodicity of the problem.

Equation (1) is solved by applying the MOM in Galerkin form. The unknown current density  $\vec{J}$  is expanded using a set of  $N$  Rao-Wilton-Glisson (RWG) [6] basis functions and its two derivative basis functions (described later) defined on triangular facets  $S_k$  of the surface  $S$ :

$$\vec{J} = \sum_{n=1}^N I_n f_n \tag{2}$$

where  $I_n$  are the unknown coefficients.

There are three kinds of basis function used in the paper, that is, RWG basis function, half-RWG basis function and invert-RWG basis function, as shown in Fig. 2. The last two are derived from RWG basis function:

$$f_n(\vec{r}) = \begin{cases} (l_n/2A_n^+) \rho_n^+(\vec{r}), & \vec{r} \text{ inside } T_n^+ \\ (l_n/2A_n^-) \rho_n^-(\vec{r}), & \vec{r} \text{ inside } T_n^- \\ 0, & \text{otherwise} \end{cases} \tag{3}$$

where  $l_n$  is the length of the common edge, and  $A_n^\pm$  is the area of triangle  $T_n^\pm$ . Vector  $\rho_n^-$  connects the observation point  $\vec{r}$  to the free vertex of the minus triangle. Vector  $\rho_n^+$  connects the free vertex of plus triangle to the observation point. There is something worth noting

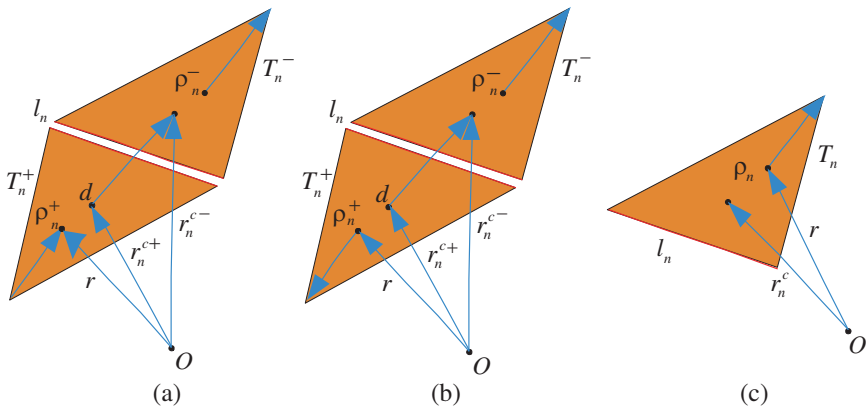


**Figure 2.** Three kinds of basis function. (a) RWG basis function. (b) Invert-RWG basis function. (c) Half-RWG basis function.

that, for invert-RWG basis functions, the observation point  $\vec{r}$  in  $T_n^+$  is directed toward the free vertex. The red line stands for the common edge of two triangles. The common edges do not always overlap. As long as the two edges have the same length, and meet a specific physical relationship, then they can build a common edge. This is usually used to deal with the current continuity of the surface meshes at the periodic boundary (PB).

### 3. 2-D PERIODIC GREEN'S FUNCTION AND ITS EWALD TRANSFORMATION

In the spatial domain, the periodic Green's function  $G_p(\vec{r}, \vec{r}_s)$  has the form

$$G_p(\vec{r}, \vec{r}_s) = \sum_{m=-\infty}^{\infty} \sum_{n=-\infty}^{\infty} e^{-j\vec{k} \cdot \vec{\rho}_{mn}} \frac{e^{-jk_0 R_{mn}}}{4\pi R_{mn}} \quad (4)$$

where

$$\begin{aligned} \vec{\rho}_{mn} &= m \cdot a_1 + n \cdot a_2 \\ R_{mn} &= |\vec{r} - \vec{r}_s - \vec{\rho}_{mn}| \end{aligned}$$

here  $\vec{\rho}_{mn}$  is the translation vector of the lattice.

In the spectral domain,  $G_p(\vec{r}, \vec{r}_s)$  becomes

$$G_p(\vec{r}, \vec{r}_s) = \sum_{m=-\infty}^{\infty} \sum_{n=-\infty}^{\infty} \frac{e^{-j\vec{k}_{tmn} \cdot (\vec{\rho} - \vec{\rho}_s)}}{2jAk_{zmn}} e^{-jk_{zmn}|z-z_s|} \quad (5)$$

where  $A = |a_1 \times a_2|$  is the cross-sectional area of the unit cell,

$$\begin{aligned} \vec{r} &= \vec{\rho} + z \cdot \hat{z} \\ \vec{k}_{tmn} &= \vec{k}_{t00} + \frac{2\pi}{A} [m(a_2 \times \hat{z}) + n(\hat{z} \times a_1)] \end{aligned}$$

is the reciprocal lattice vector.

$$k_{zmn} = \sqrt{k_0^2 - \vec{k}_{tmn} \cdot \vec{k}_{tmn}},$$

where  $\text{Re}(k_{zmn}) \geq 0$ ,  $\text{Im}(k_{zmn}) \leq 0$ .

#### 3.1. Ewald Transformation of PGF

The spatial and spectral formulations of PGF are slowly convergent. However, the Ewald method successfully combines both formulations into fast converging series. Here, we present the details of the Ewald transform used to compute the potential GFs of a periodic structure

with general skewed lattice. The Ewald transformation starts from the spatial domain representation of the PGF [Eq. (4)] and makes use of the identity

$$\frac{e^{-jkR_{mn}}}{R_{mn}} = \frac{2}{\sqrt{\pi}} \int_0^\infty e^{-R_{mn}^2 s^2 + \frac{k_0^2}{4s^2}} ds \quad (6)$$

where  $s$  is a complex variable. In order that the integrand converges as  $s \rightarrow 0$  for a wavenumber  $k_0$  with an arbitrary amount of loss, the path is chosen so that  $\arg(s) = \pi/4$  as  $s \rightarrow 0$ . In order to have convergence as  $s \rightarrow \infty$ , the path is chosen so that  $-\pi/4 \leq \arg(s) \leq \pi/4$ . Next, (6) is substituted into (4) and the integral is split into two terms, as

$$G_p(r, r') = G_{p1}(r, r') + G_{p2}(r, r') \quad (7)$$

where

$$G_{p1}(r, r') = \frac{1}{4\pi} \sum_{m=-\infty}^{\infty} \sum_{n=-\infty}^{\infty} e^{-jk_{t00} \cdot \rho_{mn}} \times \frac{2}{\sqrt{\pi}} \int_0^E e^{-R_{mn}^2 s^2 + \frac{k_0^2}{4s^2}} ds \quad (8)$$

$$G_{p2}(r, r') = \frac{1}{4\pi} \sum_{m=-\infty}^{\infty} \sum_{n=-\infty}^{\infty} e^{-jk_{t00} \cdot \rho_{mn}} \times \frac{2}{\sqrt{\pi}} \int_E^\infty e^{-R_{mn}^2 s^2 + \frac{k_0^2}{4s^2}} ds \quad (9)$$

Using the identity [16, Eq. (7.7.7)]

$$\begin{aligned} \frac{2}{\sqrt{\pi}} \int_E^\infty e^{-R_{mn}^2 s^2 + \frac{k_0^2}{4s^2}} ds &= \frac{1}{2R_{mn}} \left[ e^{-jk_0 R_{mn}} \operatorname{erfc} \left( R_{mn} E - \frac{jk}{2E} \right) \right. \\ &\left. + e^{jk_0 R_{mn}} \operatorname{erfc} \left( R_{mn} E + \frac{jk}{2E} \right) \right] \end{aligned} \quad (10)$$

where  $\operatorname{erfc}$  is the complementary error function,  $G_{p2}(r, r')$  can be written as

$$\begin{aligned} G_{p2}(r, r') &= \sum_{m=-\infty}^{\infty} \sum_{n=-\infty}^{\infty} \frac{e^{-jk_{t00} R_{mn}}}{4\pi R_{mn}} \\ &\times \operatorname{real} \left[ e^{jk_0 R_{mn}} \operatorname{erfc} \left( R_{mn} E + \frac{jk}{2E} \right) \right] \end{aligned} \quad (11)$$

which is essentially a “modified” spatial-domain part of the PGF. Making use of the Poisson transformation [17, 18], Eq. (8) is finally transformed as

$$\begin{aligned} G_{p1}(r, r') &= \sum_{m=-\infty}^{\infty} \sum_{n=-\infty}^{\infty} \frac{e^{-jk_{tmn} \cdot (\rho - \rho')}}{4j A k_{zmn}} \\ &\times \left[ e^{-jk_{zmn}(z-z')} \operatorname{erfc} \left( \frac{jk_{zmn}}{2E} - (z-z') E \right) \right. \\ &\left. + e^{jk_{zmn}(z-z')} \operatorname{erfc} \left( \frac{jk_{zmn}}{2E} + (z-z') E \right) \right] \end{aligned} \quad (12)$$

### 3.2. Optimum Splitting Parameter $E$

By analysis of the asymptotic behavior of the series terms, the approximation to the optimal value for 2-D general skewed lattices is given by [13, 19]:

$$E = \max \left( \sqrt{\frac{\pi}{A}}, \frac{k}{2H} \right) \tag{13}$$

where  $H^2$  is the maximum exponent permitted. For example, consider a worst case in which there is no phasing ( $k_{x0} = k_{y0} = 0$ ). If we require  $H^2 = 9$  we need  $E > k/2H \approx k/6 \approx 1/\lambda$ . In other words, for  $H^2 = 9$ , the choice of the optimum parameter  $E = \sqrt{\pi/A}$  is a good choice if  $A < 3\lambda^2$ . Choosing this value and adjusting the summation limits so that the most dominant terms are kept, in almost all practical cases it is sufficient to include only nine summation terms in (11) and (12) (i.e., the summation limits are from  $-1$  to  $+1$ ), in which the error level is usually less than 0.1%.

### 3.3. Extraction of the Singular Term of PGF

By extracting its singularity [20], the periodic Green's function (PGF) can be expressed as  $G_p = G_{p1} + [G_{p2} - 1/(4\pi R)] + 1/4\pi R$ . The singularity subtraction technique [21] used in this paper can compute the singularity of  $|r - r'|^n$  ( $n \geq -3$ ) type. The remaining part using L'Hospital rule has a finite value at  $R \rightarrow 0$  since:

$$\begin{aligned} & \lim_{R \rightarrow 0} \left\{ \frac{1}{8\pi R} \sum_{\pm} e^{\pm jkR} \operatorname{erfc} \left( RE \pm \frac{jk}{2E} \right) - \frac{1}{4\pi R} \right\} \\ &= \frac{jk}{4\pi} \cdot \left[ \operatorname{erfc} \left( \frac{jk}{2E} \right) - 1 \right] - \frac{E}{2\pi\sqrt{\pi}} e^{\frac{k^2}{4E^2}} \end{aligned} \tag{14}$$

where the real part of  $\operatorname{erfc}(jk/2E)$  equates to 1.

## 4. INTERPOLATION OF PGFS

In the following, the interpolation procedure of PGFs is introduced. PGF values are pre-computed at each frequency point and tabulated in a rectangular 3-D grid along  $x-x'$ ,  $y-y'$ , and  $z-z'$ . The GF values needed to compute the numerical integrals in the MoM matrix are then retrieved from the table using interpolation routines (quadrature interpolation). This is computationally very advantageous. The reason is in the fact that interpolating the GF values from the table is much faster than computing the Ewald sums directly (since this has to

be done for every pair of source and field triangles in the numerical integration using cubature formulas.)

The relative error  $\varepsilon$  obtained by interpolating the PGFs is defined as

$$\varepsilon = \left| \frac{G^{\text{int}} - G^{\text{ex}}}{G^{\text{ex}}} \right|$$

where  $G^{\text{int}}$  and  $G^{\text{ex}}$  are the interpolated and the exact data, respectively. The exact data are obtained by calculating the series (11) and (12) with an accuracy  $\varepsilon = 10^{-7}$ ; the relative errors less than  $\varepsilon = 10^{-7}$  have therefore been neglected.

We take the 2-D metallic structure with orthogonal lattices shown in Fig. 3 (a) as example. The threshold of far interaction between field and source triangles usually is set to  $\lambda/10$ . When  $|r - r'| < \lambda/10$ , PGF change dramatically and its singularity must be extracted. For the near interaction, the 2-D grid is in  $-0.1\lambda < \Delta x < 0.1\lambda$ ,  $-0.1\lambda < \Delta y < 0.1\lambda$ ,  $z - z' = 0$ ; For far interaction, the 2-D grid is in  $-|a_1| < \Delta x < |a_1|$ ,  $-|a_2| < \Delta y < |a_2|$ ,  $z - z' = 0$ , shown in Fig. 3(b). The red line stands for the singular boundary, so the PGFs at the center of sub-grid generally are pre-computed and stored. In Fig. 4, an example is shown of the relative error in the interpolation of PGF involved far and near interaction through quadrature interpolation, with various values of int  $N_{\text{int}}$ . An extensive number of comparisons have also been performed to estimate the accuracy reached with different numbers of interpolation points. In Fig. 5, signs (A...L) are the sampling points for interpolation. A very high level of accuracy is anyway easily obtained with a relatively small number of interpolation points. The side length range of the sub-grid usually is  $0.015 \sim 0.03\lambda$ , and the higher interpolation accuracy ( $\varepsilon < 10^{-3}$ , even  $10^{-5}$ ) can be obtained.

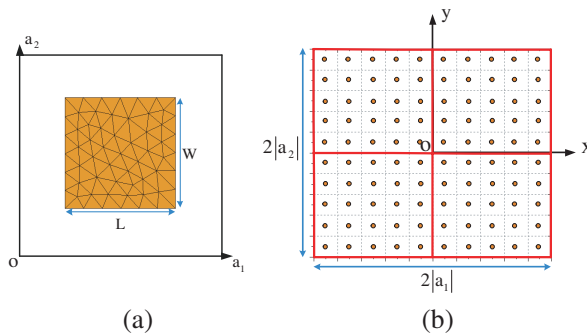


**Figure 3.** The PGFs at the center of sub-grids (yellow point) will be pre-computed and stored: (a) The unit cell of FSS. (b) A rectangular 2-D grid with  $N_{\text{int}} \times N_{\text{int}}$  sub-grids.

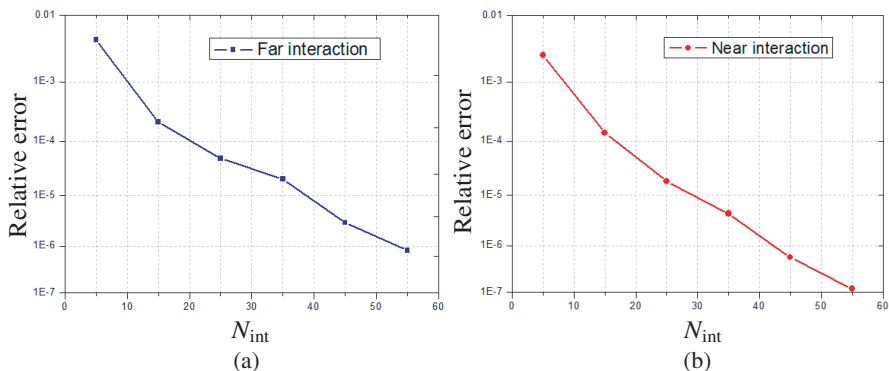


**Figure 4.** The relative error of a single point. Reference structure: primitive vector  $a_1 = a_2 = 0.55\lambda$ ; phase shifts  $k_{x0} = \sqrt{6}k_0/4$ ,  $k_{y0} = \sqrt{2}k_0/4$ . Accuracy reached interpolating PGFs through quadratic interpolation, with a 2-D grid of  $N_{\text{int}} \times N_{\text{int}}$  equispaced points in  $-0.55\lambda < \Delta x < 0.55\lambda$ ,  $-0.55\lambda < \Delta y < 0.55\lambda$ ,  $z - z' = 0$ . (a) Far-interaction  $r - r' = (/ - 0.21\lambda, 0.29\lambda, 0/)$ . (b) Near-interaction  $r - r' = (/ - 0.011\lambda, 0.018\lambda, 0/)$ .

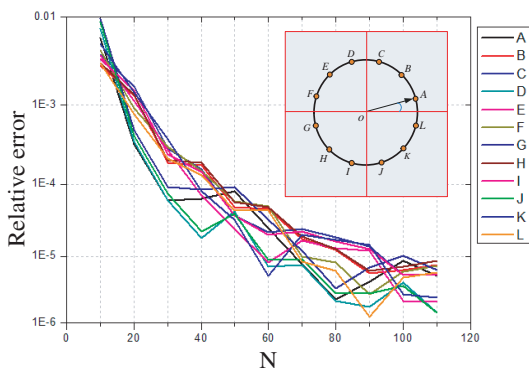


**Figure 5.** The relative error of a series of points. Reference structure: primitive vector  $a_1 = a_2 = 0.45\lambda$ ; phase shifts  $k_{x0} = k_0/4$ ,  $k_{y0} = \sqrt{3}k_0/4$ . Accuracy reached interpolating PGFs through quadratic interpolation, with a 2-D grid of  $N_{\text{int}} \times N_{\text{int}}$  equispaced points in  $-0.45\lambda < \Delta x < 0.45\lambda$ ,  $-0.45\lambda < \Delta y < 0.45\lambda$ . The data plotted refer to the circular line  $(x - x')^2 + (y - y')^2 = (0.23\lambda)^2$ ,  $z - z' = 0$ ; The number of sampling point is 12, the first one (Point A) starts from  $\varphi = 15^\circ$ .

For the case of FSS under the normal incidence of plane wave, because the phase shift factor is zero, PGF value is just related to  $|r - r'|$ . For the near interaction, the 2-D grid is in  $0 < \Delta x < 0.1\lambda$ ,  $0 < \Delta y < 0.1\lambda$ ,  $z - z' = 0$ ; For far interaction, the 2-D grid is in  $0 < \Delta x < |a_1|$ ,  $0 < \Delta y < |a_2|$ ,  $z - z' = 0$ . The number of pre-computed PGFs can be reduced to 1/4 of the original one.

## 5. FSS UNIT CONNECTING TO PERIODIC BOUNDARY (PB)

This case usually appears in aperture periodic structure shown in Fig. 6. The triangle meshes connecting to the periodic boundary (PB) requires special handling. A possible imposition of periodic boundary condition (PBC) to the surface mesh has been discussed in detail in [22]. The basic observation is that the fields on the PB of a surface mesh are related to the fields on the opposite PB through a phase relation. If the unknown field at an edge on one of the PBs is  $e_m$ , the value  $e_n$  of the field at the corresponding edge on the opposition PB is given by

$$e_n = e_m \cdot e^{-j\vec{k}_{t00} \cdot \Delta\vec{r}}$$

where  $\Delta\vec{r} = (a_1 \text{ or } a_2)$  is the vector joining the two edges.

The two triangles (red line) at the left and right PB respectively constitute a RWG edge. Similarly, the two triangles (green line) at the up and low PB respectively constitute a RWG edge. This relation requires that the surface meshes of the opposite PBs be identical.

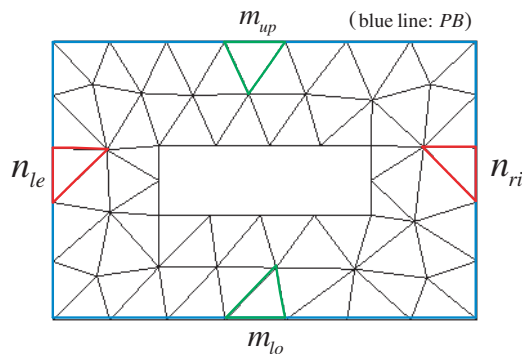


**Figure 6.** The triangle mesh connecting to PB.

## 6. USING LATTICE SYMMETRY TO SIMPLIFY THE GEOMETRY MODEL

Here we take the aperture periodic structure shown in Fig. 7 for example, because the aperture structure is relatively complex. The triangle meshes connecting to the periodic boundary (PB) require special handling.

### 6.1. Regular Array Under Normal Incident of Plane Wave

Suppose FSS is under the normal incidence of plane wave with the  $E$ -field parallel to the  $x$ -axis ( $TEM_x$ ). The geometry model was simplified to 1/4 of original one using the lattice symmetry (Fig. 8). The time of filling MOM matrix and solving linear system by iterative method is reduced approximately to 1/4 of original one.

In addition to the primary source triangle, the coordinates of other three source triangles can be obtained through mirror. The relationship for the current expansion coefficients of the four source triangles is as follows:

$$I_1 = -I_2 = -I_3 = I_4$$

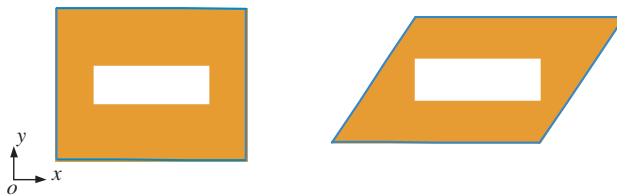


**Figure 7.** Unit cell of rectangular aperture FSS (blue line: PB).

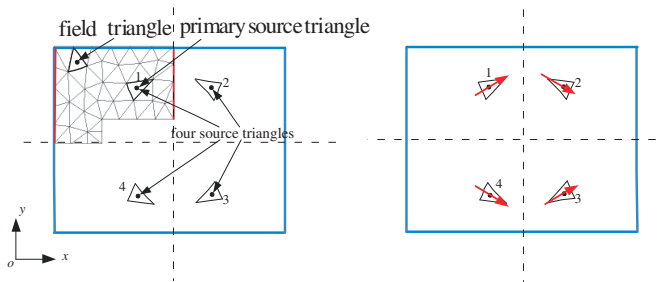


**Figure 8.** The field and source triangles. Red arrows are the current direction of the four source triangles.

The impedance matrix of the mixed-potential integral equation (MPIE) is given by

$$Z_{mn} = \sum_{k=1}^4 c(k) \cdot \left\{ j\omega \langle f_m, \vec{G}_A \otimes f_{nk} \rangle + \frac{1}{j\omega} \langle \nabla \cdot f_m, G_V \otimes (\nabla' \cdot f_{nk}) \rangle \right\}$$

where

$$c(k) = \begin{cases} 1, & \text{if } k = 1 \text{ or } 4 \\ -1, & \text{if } k = 2 \text{ or } 3 \end{cases}$$

That is, one field triangle corresponds to four source triangles.  $f_{n1}$  is the basis function of primary source triangle  $n_1$ ;  $f_{n2}$ ,  $f_{n3}$  and  $f_{n4}$  are the basis function of the other three source triangles ( $n_2$ ,  $n_3$ ,  $n_4$ ), respectively.

The triangle meshes connecting to left and right edges (red line) should be assigned half-RWG basis function, because there is a current flowing through left and right edges. There is no current following through upper and lower edges, so the two edges can be considered as the open boundary edges.

## 6.2. Regular Array Under Oblique Incident of Plane Wave

Suppose FSS is under the oblique incidence of plane wave ( $xoz$ -plane is the incident plane) with  $V$ -polarization and  $H$ -polarization respectively.  $V$ -polarization denotes the  $E$ -field parallel to the incident plane;  $H$ -polarization denotes the  $E$ -field perpendicular to the incident plane. The geometry model was simplified to 1/2 of the original one using the lattice symmetry (Fig. 9). The time of filling MOM matrix and solving linear system by iterative method is reduced approximately to 1/2 of the original one.

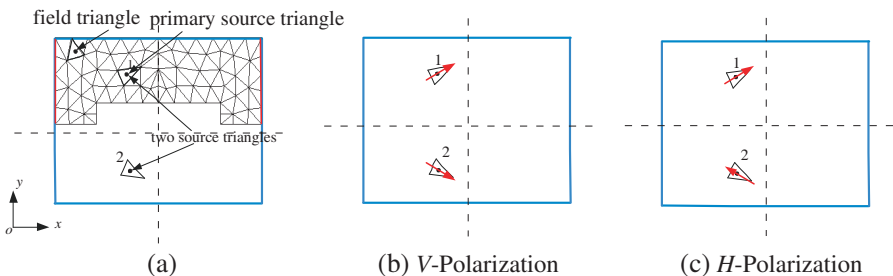


**Figure 9.** The field and source triangles. Red arrows are the current direction of the two source triangles.

The relationship between current expansion coefficients of two source triangles is as follows:

$$I_1 = \begin{cases} I_2, & \text{if } V\text{-Polarization} \\ -I_2, & \text{if } H\text{-Polarization} \end{cases}$$

The impedance matrix of the mixed-potential integral equation (MPIE) is given by

V-Polarization :

$$Z_{mn} = \sum_{k=1}^2 j\omega \langle f_m, \vec{G}_A \otimes f_{nk} \rangle + \frac{1}{j\omega} \langle \nabla \cdot f_m, G_V \otimes (\nabla' \cdot f_{nk}) \rangle$$

H-Polarization :

$$Z_{mn} = \sum_{k=1}^2 c(k) \cdot \left\{ j\omega \langle f_m, \vec{G}_A \otimes f_{nk} \rangle + \frac{1}{j\omega} \langle \nabla \cdot f_m, G_V \otimes (\nabla' \cdot f_{nk}) \rangle \right\}$$

where

$$c(k) = \begin{cases} 1, & \text{if } k = 1 \\ -1, & \text{if } k = 2 \end{cases}$$

The triangle meshes connecting to left and right edges (red line) should be assigned RWG basis function. In the case of V-polarization, there is no current following through upper and lower edges, so the two edges can be considered as the open boundary edges. In the case of H-polarization, the triangle meshes at the upper and lower edges should be assigned half-RWG basis function, due to the existing current following through the two edges.

### 6.3. Skewed Array under Normal Incident of Plane Wave

Supposed FSS is under the normal incidence of plane wave with the E-field parallel to the x-axis (TEM<sub>x</sub>). The geometry model was simplified to 1/2 of original one using the lattice symmetry (Fig. 10).

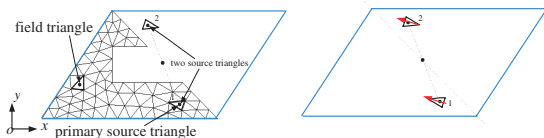


**Figure 10.** The field and source triangles. Red arrows are the current direction of the two source triangles.

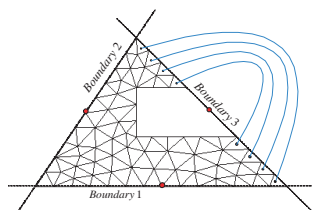


**Figure 11.** Invert-RWG consisting of two corresponding triangles.

The time of filling MOM matrix and solving linear system by iterative method is reduced approximately to 1/2 of original one.

The relationship between current expansion coefficients of two source triangles is as follow

$$I_1 = -I_2$$

The impedance matrix of the mixed-potential integral equation (MPIE) is given by

$$Z_{mn} = \sum_{k=1}^2 c(k) \cdot \left\{ j\omega \langle f_m, \vec{G}_A \otimes f_{nk} \rangle + \frac{1}{j\omega} \langle \nabla \cdot f_m, G_V \otimes (\nabla' \cdot f_{nk}) \rangle \right\}$$

where

$$c(k) = \begin{cases} 1, & \text{if } k = 1 \\ -1, & \text{if } k = 2 \end{cases}$$

In this case, there are currents following through the three patch edges. Take the third edge of the patch (Boundary 3) for example, as shown in Fig. 11. Two triangles connected by the blue line constitute an invert-RWG basis function. The third edge of the patch has 4 invert-RWGs. Two interior edges of the invert-RWG are symmetrical about the center of patch edge (red dot). The triangles at the first and second edge of the patch constitute the invert-RWG in the same way, which have 7 and 5 invert-RWGs respectively. If the number of triangles at the patch edge is odd, the triangle at the center of the patch edge should be assigned half-RWG.

## 7. NUMERICAL EXAMPLES

### 7.1. Jerusalem Cross

In the first example, we consider the problem of a free-standing planar array of perfectly conducting Jerusalem-Cross shaped patch shown in Fig. 12. Fig. 13 shows the reflection coefficient for the Floquet TEM mode with the electric field oriented in the  $x$ -direction ( $TEM_x$ ). The number of terms in both Ewald sums is set to 9. Further increasing the number of terms does not show any changes in the reflection coefficient. The one-4th model is discretized into 80 triangles in the whole frequency band. We compare the results obtained using our approach (black solid line) with the results obtained using the spectral-domain approach [1] (Blue ring) and the numerical values taken from [13] (red solid line). Good agreement with the reference results can be observed in the reflection coefficient.

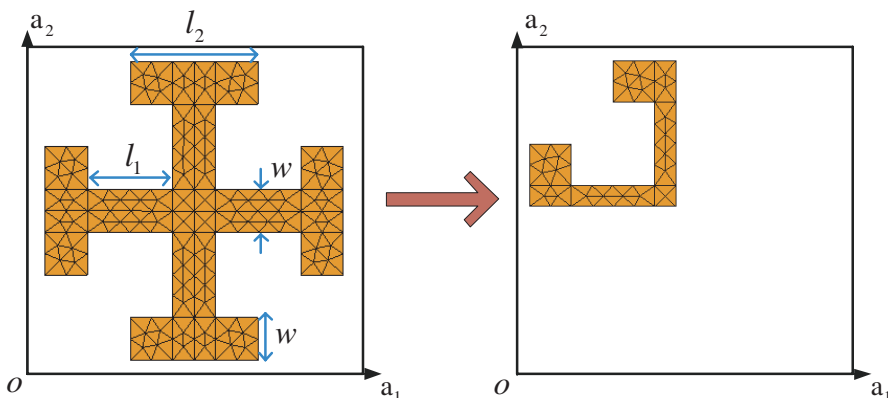


**Figure 12.** The unit model of Jerusalem cross array is simplified to one-4th model. Dimension are in millimeters:  $w = 1.9$ ,  $l_1 = 3.8$ ,  $l_2 = 5.7$ ,  $a_1 = a_2 = 15.2$ .

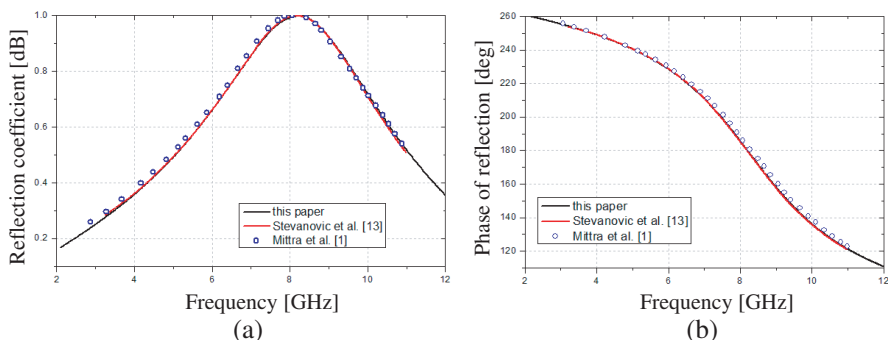


**Figure 13.** (a) Magnitude. (b) Phase of the reflection coefficient.

### 7.2. Double Square-loop

This example involves a double-square-loop periodic structure defined on a 9.5588 mm square grid. The dimensions of the element are shown in Fig. 14. The incident field has center frequency  $f_c = 14.5$  GHz, bandwidth  $f_{bw} = 7$  GHz, and illuminates the screen from the  $(\theta^{inc} = 30^\circ, \phi^{inc} = 0^\circ)$  direction with  $V$ -polarization and the  $(\theta^{inc} = 45^\circ, \phi^{inc} = 0^\circ)$  direction with  $H$ -polarization, respectively. Fig. 15 shows the reflection and transmission coefficients of the structure. Black solid line and blue solid line represent the reflection and transmission coefficients obtained using our technique, respectively; Red-ring and green dashed lines represent the results using the simulation technique

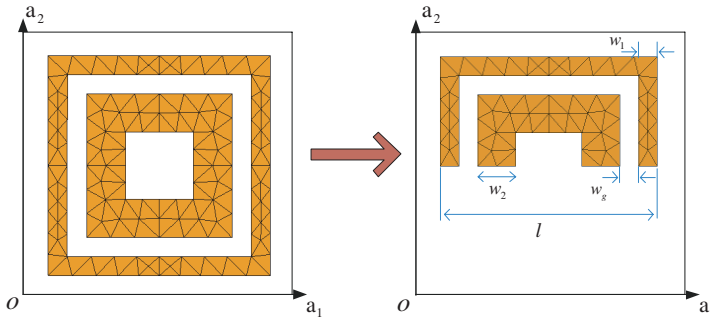


**Figure 14.** The unit model of double square-loop array is simplified to one-2nd model. Dimension are in millimeters:  $w_1 = w_g = 0.5588$ ,  $w_2 = 1.125$ ,  $l = 6.4588$ ,  $a_1 = a_2 = 9.5588$ .

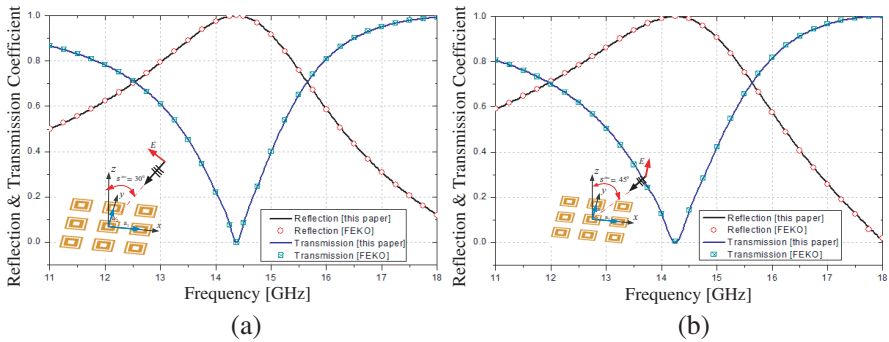


**Figure 15.** Reflection and transmission coefficient. (a) Incident direction ( $\theta^{\text{inc}} = 30^\circ$ ,  $\phi^{\text{inc}} = 0^\circ$ ) with  $V$ -polarization. (b) Incident direction ( $\theta^{\text{inc}} = 45^\circ$ ,  $\phi^{\text{inc}} = 0^\circ$ ) with  $H$ -polarization.

of EMSS FEKO. Very good agreement with the reference results of FEKO can be observed. Here, the one-2nd model is discretized into 100 triangles, and the number of terms in both Ewald sums is set to 9.

### 7.3. Conducting Screen Perforated with Circular Holes

The transmission of a plane wave incident on a thin perfectly conducting screen perforated periodically with circular holes is considered. The geometry of the problem is defined in the inset of Fig. 17 that shows the geometry layout of the 2-D array of circular holes in thin conducting screen. The dimensions of the element are shown in Fig. 16. The reflection and transmission coefficients for a plane wave

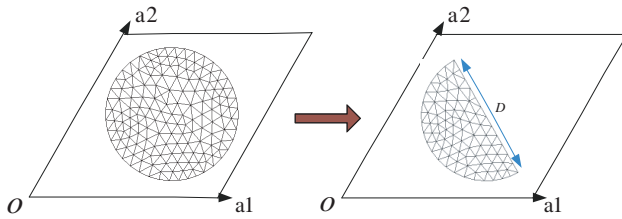


**Figure 16.** The unit model of circular aperture array is simplified to one-2nd model. Dimension are in millimeters:  $D = 12$ ,  $a_1 = a_2 = 10\sqrt{3}$  and  $\alpha = 60^\circ$ .

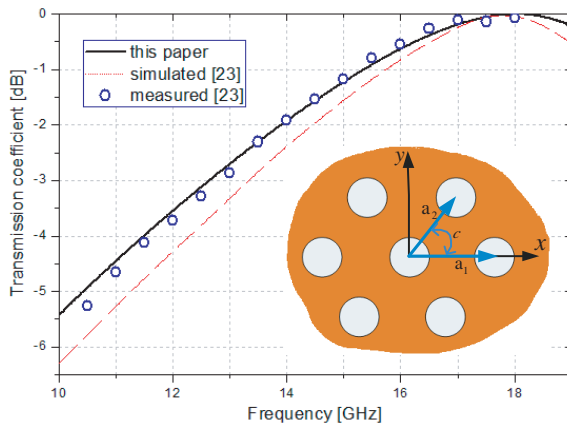


**Figure 17.** Transmission coefficient.

with the  $E$ -field parallel to the  $y$ -axis at normal incidence are plotted as the function of frequency in Fig. 17. The results obtained using the presented method (black solid lines) are compared to the simulations (red dot lines) and measured values (blue ring) taken from [23]. A very good agreement with the measured values [23] can be noticed. Here, only nine terms in both Ewald sums give the convergent results for a mesh density of one-2nd model with 108 triangular cells.

### 7.4. Cross-Shaped Quasi-Optical Filter

Finally, we analyze the bandpass filter formed by periodic cross-shaped holes with a resonance frequency of 280 GHz shown in Fig. 18 [24]. The one-4th model is discretized into 218 triangles to ensure accurate results obtained in the entire frequency band. The transmission coefficients for a plane wave with the  $E$ -field parallel to the  $x$ -axis at normal incidence

( $TEM_x$  mode) are plotted as a function of frequency in Fig. 19. Black solid lines represent the results obtained using our technique, red solid lines represent the results using the simulation technique of [24], and the measured values are denoted via ring (o). Very good agreement with the reference results can be observed. Since simulation relative bandwidth is very wide and the value of the splitting parameter may be unbalanced, we need more terms in the spectral sum (49) than in the spatial one (9) to ensure the GF convergence [13]. The time needed to solve this structure is 6.3 s per frequency point on a PC with Intel core i5 2.8-GHz processor, 4 GB of RAM, and Microsoft Win7 operating system. The corresponding CPU time on the same PC is 122 s and 896 s per frequency point for Ansoft Designer and EMSS FEKO, respectively.

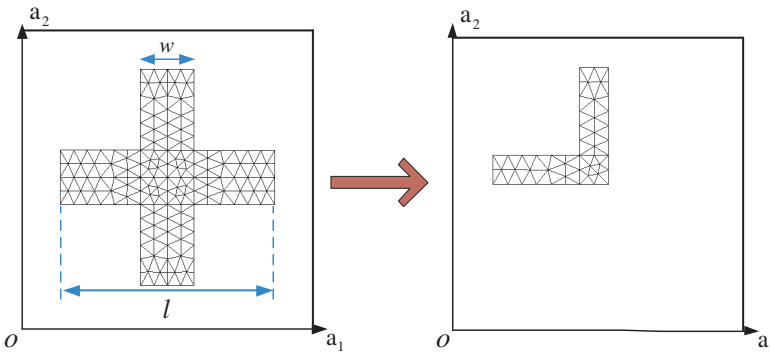


**Figure 18.** The unit model of cross-shaped aperture array is simplified to one-4th model. Dimension are in micrometers: Square lattice period  $a_1 = a_2 = 810$ , slot length  $l = 570$ , slot width  $w = 160$ .

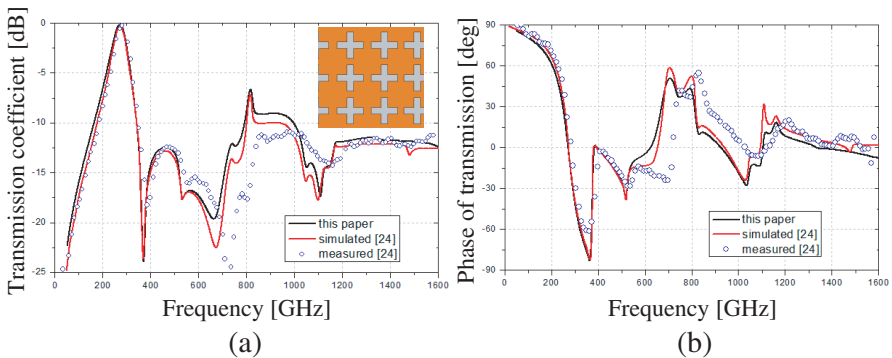


**Figure 19.** (a) Magnitude. (b) Phase of the transmission coefficient.

## 8. CONCLUSION

We propose a spatial-domain integral-equation method for the analysis of frequency selective surfaces (FSS) using Ewald transformation and lattice symmetry. The method uses Ewald's acceleration technique to speed up the convergence of the GFs. Moreover, we use the lattice symmetry to simplify the unit model and the unknowns are reduced greatly, so that the solving time of MoM linear system and the matrix-filling time are reduced dramatically. Two new basis functions deriving from RWG basis function are introduced to deal with the current condition of the unit patch. A number of periodic structures with general skewed lattices under oblique and normal incidence plane-wave excitations are studied. The simulations show that, in most cases, only nine terms in both Ewald sums suffice to obtain results that agree very well with the measured or numerical results reported in the literatures. Therefore, it shows that our technique is an accurate and efficient method for analyzing periodic structures. Extension of the proposed approach to the analysis of arbitrary complicated periodic structures by using volume-surface integral equation (VSIE) [25–27] and adaptive cross approximation (ACA) [28] is feasible and under development.

## ACKNOWLEDGMENT

This work is funded by the National Natural Science Foundation of China under Grant 60871003 and 60801008.

## REFERENCES

1. Mittra, R., C. H. Chan, and T. Cwik, "Techniques for analyzing frequency selective surfaces — A review," *Proc. IEEE*, Vol. 76, No. 12, 1593–1615, Dec. 1988.
2. Duan, Z., B.-I. Wu, S. Xi, H. Chen, and M. Chen, "Research progress in reversed cherenkov radiation in double-negative metamaterials," *Progress In Electromagnetics Research*, Vol. 90, 75–87, 2009.
3. Catedra, M. F. and R. P. Torres, "A scheme to analyze scattering from flat metallic periodic structures using the conjugate-gradient and the fast fourier transform method," *Progress In Electromagnetics Research*, Vol. 4, 315–343, 1991.
4. Chen, C.-C., "Diffraction of electromagnetic waves by a conducting screen perforated periodically with circular holes," *IEEE Trans. Microw. Theory Tech.*, Vol. 19, No. 5, 475–481, May 1971.

5. Wu, T. K., *Frequency Selective Surface and Grid Array*, Wiley, New York, 1995.
6. Rao, S. M., D. R. Wilton, and A. W. Glisson, "Electromagnetic scattering by surface of arbitrary shape," *IEEE Trans. Antennas Propag.* Vol. 30, 409–411, 1982.
7. Collin, R. E., *Field Theory of Guided Waves*, IEEE Press, New York, 1991.
8. Collin, R. E. and F. J. Zucker, *Antenna Theory*, Ch. 19 and 20, Mc-Graw-Hill, New York, 1969.
9. Jorgenson, R. E. and R. Mittra, "Efficient calculation of the free-space periodic Green's function," *IEEE Trans. Antennas Propag.*, Vol. 38, No. 5, 633–642, May 1990.
10. Singh, S., W. F. Richards, J. R. Zinecker, and D. R. Wilton, "Accelerating the convergence of series representing the free periodic Green's function," *IEEE Trans. Antennas Propag.*, Vol. 38, No. 12, 1958–1962, Dec. 1990.
11. Singh, S. and R. Singh, "On the use of  $\rho$ -algorithm in series acceleration," *IEEE Trans. Antennas Propag.*, Vol. 39, No. 10, 1514–1517, Oct. 1991.
12. Ewald, P. P., "Die berechnung optischer und elektrostatischer gitterpotentiale," *Ann. Phys.*, Vol. 64, 253–287, 1921, Translated by A. Cornell, Atomics International Library, 1964.
13. Stevanovic, I., P. Crespo-Valero, K. Blagovic, F. Bongard, and J. R. Mosig, "Integral-equation analysis of 3-D metallic objects arranged in 2-D lattices using the Ewald transformation," *IEEE Trans. Antennas Propag.*, Vol. 54, No. 10, 3688–3697, Oct. 2006.
14. Mathis, W. and A. F. Peterson, "Efficient electromagnetic analysis of a doubly infinite array of rectangular apertures," *IEEE Trans. Microw. Theory Tech.*, Vol. 46, No. 1, 46–54, Jan. 1998.
15. Eibert, T. F., J. L. Volakis, D. R. Wilton, and D. R. Jackson, "Hybrid FE/BI modeling of 3-D doubly periodic structures utilizing triangular prismatic elements and an MPIE formulation accelerated by the Ewald transformation," *IEEE Trans. Antennas Propag.*, Vol. 47, No. 5, 843–850, May 1999.
16. Olver, F. W. J., D. W. Lozier, R. F. Boisvert, and C. W. Clark, *NIST Handbook of Mathematical Functions*, Cambridge University Press, New York, 2010.
17. Kinayman, N. and M. I. Aksun, "Comparative study of acceleration techniques for integrals and series in electromagnetic problems," *Radio Sci.*, Vol. 30, No. 6, 1713–1722, Nov./Dec. 1995.

18. Ewald, P. P., "Dispersion und doppelbrechung von elektronengittern (kristallen)," Dissertation, Munchen, 1912, also *Ann. Phys.*, Vol. 49, 1, 1916.
19. Jordan, K. E., G. R. Richter, and P. Sheng, "An efficient numerical evaluation of the Green's function for the Helmholtz operator on periodic structures," *J. Comp. Phys.*, Vol. 63, 222–235, 1986.
20. Stevanovic and Mosig, "Periodic Green's function for skewed 3-d lattices using the Ewald transformation," *Microwave and Opt. Tech. Letters*, Vol. 49, No. 6, 1353–1357, Jun. 2007.
21. Hanninen, I., M. Taskinen, and J. Sarvas, "Singularity subtraction integral formulae for surface integral equations with rwg, rooftop and hybrid basis functions," *Progress In Electromagnetics Research*, Vol. 63, 243–278, 2006.
22. McGrath, D. T. and V. P. Pyati, "Phased array antenna analysis with the hybrid finite element method," *IEEE Trans. Antennas Propag.*, Vol. 42, No. 12, 1625–1630, 1994.
23. Chen, C.-C., "Diffraction of electromagnetic waves by a conducting screen perforated periodically with circular holes," *IEEE Trans. Microw. Theory Tech.*, Vol. 19, No. 5, 475–481, May 1971.
24. Bozzi, M., L. Perregrini, J. Weinzierl, and C. Winnewisser, "Efficient analysis of quasi-optical filters by a hybrid MoM/BI-RME method," *IEEE Trans. Antennas Propag.*, Vol. 49, No. 7, 1054–1064, Jul. 2001.
25. Li, M. and W. C. Chew, "Applying divergence-free condition in solving the volume integral equation," *Progress In Electromagnetics Research*, Vol. 57, 311–333, 2006.
26. Fan, Z., R.-S. Chen, H. Chen, and D.-Z. Ding, "Weak form nonuniform fast fourier transform method for solving volume integral equations," *Progress In Electromagnetics Research*, Vol. 89, 275–289, 2009.
27. Shi, Y., X. Luan, J. Qin, C. Lv, and C.-H. Liang, "Multilevel Green's function interpolation method solution of volume/surface integral equation for mixed conducting/bi-isotropic objects," *Progress In Electromagnetics Research*, Vol. 107, 239–252, 2010.
28. Zhao, K., M. N. Vouvakis, and J. F. Lee, "The adaptive cross approximation algorithm for accelerated method of moments computations of EMC problems," *IEEE Trans. EMC*, Vol. 47, No. 4, 763–773, Nov. 2005.